

Track Recognition for the $\Delta E - E$ Telescope with Silicon Strip Detectors

Fenhai Guan^{a,*}, Yijie Wang^a, Xinyue Diao^a, Yuhao Qin^a, Zhi Qin^a, Dong Guo^a, Qianghua Wu^a, Dawei Si^a, Sheng Xiao^a, Yaopeng Zhang^a, Xuan Zhao^a, Zhigang Xiao^{a,**}

^aDepartment of Physics, Tsinghua University, Beijing 100084, China

Abstract

For the high granularity and high energy resolution, Silicon Strip Detector (SSD) is widely applied in assembling telescopes to measure the charged particles in heavy ion reactions. In this paper, we present a novel method to achieve the track recognition in the SSD telescopes of the Compact Spectrometer for Heavy Ion Experiment (CSHINE). Each telescope consists of a single-sided silicon strip detector (SSSSD) and a double-sided silicon strip detector (DSSSD) backed by 3×3 CsI(Tl) crystals. Detector calibration, track reconstruction and coordinate transformation are implemented. Special decoding algorithm is developed for the multi track recognition procedure to deal with the multi-hit effect convoluted by charge sharing and the missing signals with certain probability. It is demonstrated that the track recognition efficiency of the method is $\sim 90\%$ and $\sim 80\%$ for the DSSSD-CsI and SSSSD-DSSSD events, respectively.

Keywords: CSHINE, SSD-SSD-CsI telescopes, Silicon strip detector, Energy calibration, Particle identification, Track reconstruction, Coordinate transformation

1. Introduction

In recent years, the $\Delta E - E$ telescopes with silicon strip detectors (SSDs) or pixel detectors are widely used in nuclear reaction experiments because of the excellent energy and position resolution as well as the good particle identification capability. In terrestrial laboratories, many such large acceptance detector systems including INDRA [1, 2], LASSA [3], HiRA [4], CHIMERA [5], MUST2 [6], FRACOS [7, 8], FIZIA [9], and ChAKRA [10], etc, have been developed for the studies of nuclear reactions, nuclear structure and particle-particle correlation. In order to investigate the nuclear equation of state (nEoS), the HBT correlation, as well as the fast fission following heavy ion reactions (HIRs) [11, 12], a compact spectrometer for heavy ion experiments (CSHINE) in the Fermi energy regime has been recently built [13, 14]. CSHINE at the current stage consists of four telescopes and three large-area parallel plate avalanche counter (PPACs). The PPACs are used to measure the fission fragments while the telescopes are used to detect light charged particles (LCPs). Each CSHINE telescope consists of a single-sided silicon strip detector (SSSSD) and a double-sided silicon strip detector (DSSSD) backed by 3×3 CsI(Tl) crystals. With the SSD-SSD-CsI configuration, particle identification in a wide energy range can be achieved by the $\Delta E - E$ correlation of DSSSD-CsI and SSSSD-DSSSD.

Before conducting physical analysis, we have to reconstruct the physical event first, which mainly includes energy calibration of the detectors, particle identification and track reconstruction. In principle, the position of the incident particle is

determined by the DSSSD of the telescope in the unit of the “pixel”, the size of which is given by the strip width. However, the task of track reconstruction is somewhat complicated because of charge sharing and multi-hit effects.

In this work, we present a novel method for event reconstruction of the SSD-SSD-CsI telescopes. The paper is arranged as following. Section 2 presents the telescope structure and the detector calibration. Section 3 and Section 4 represent the track reconstruction and coordinate transformation. Section 5 represents the results of the phase space distribution of the LCPs and Section 6 is the summary.

2. Detector calibration

Both silicon strip detectors and the CsI hodoscope require calibration before physical analysis can be proceeded. While the SSD is calibrated using the conventional source plus pulser method, the CsI calibration relies on the particle type obtained from the $\Delta E - E$ plot. Before the calibration of CsI units, particle identification (PID) on $\Delta E - E$ plot has to be established. Thus, the calibration procedure is convoluted with the track recognition in the SSD telescope. This section presents the procedure of the detector calibration.

2.1. Telescope configuration

Fig. 1 shows the schematic diagram of a single CSHINE SSD-SSD-CsI telescope. Each telescope is composed of a SSSSD, a DSSSD and a hodoscope of 3×3 CsI(Tl) crystals. The SSDs are BB7 series with active areas of $63.8\text{mm} \times 63.8\text{mm}$. On each SSD surface, there are 32 strips with the width of 2 mm, and the gap between adjacent strips is 100 μm . The strips on the SSSSD surface (“1S”) and on the back-side of

*gfh16@mails.tsinghua.edu.cn (Corr. author)

**xiaozg@tsinghua.edu.cn (Corr. author)

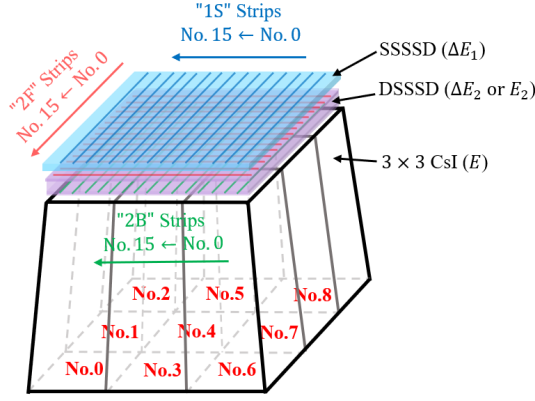


Fig. 1. (Color online) The schematic diagram of a single CSHINE telescope. Each telescope consists of a SSSSD for ΔE_1 detection, a DSSSD for ΔE_2 or E_2 detection and 3×3 CsI crystals for E detection.

Table 1: The parameters of the four CSHINE SSD telescopes. L is the distance from the detector to the target, θ_{lab} and ϕ_{lab} are polar angle and azimuthal angle of the detector center in the laboratory frame, respectively.

Telescope No.	1	2	3	4
L (mm)	315.5	275.5	275.5	215.5
θ_{lab} ($^\circ$)	18	25	31	51
ϕ_{lab} ($^\circ$)	302	218	126	81
SSSSD (μm)	304	305	110	70
DSSSD (μm)	1010	1008	526	306
CsI(Tl) (mm)	50	50	50	50

the DSSSD (“2B”) are parallel to each other and are numbered in the same order, while the “2B” strips are perpendicular to that on the front-side of the DSSSD (“2F”). In the recent experiment, every two strips are merged into one channel to reduce electronics, so there are 16 channels on each detector surface and the size of the pixel is determined to be $4 \times 4 \text{ mm}^2$ [14]. Nine trapezoidal crystals, each of which is 50 mm long, $23\text{mm} \times 23\text{mm}$ on the front and $27\text{mm} \times 27\text{mm}$ on the rear, are closely packed into one trapezoid hodoscope. The position of an particle impinging into the crystal can be determined by both the fired crystal and the fired strips on the “2B” and “2F” surfaces. With such SSD-SSD-CsI configuration, we can detect LCPs in a wide energy range. The details of the CSHINE can be found in [14]. Table 1 presents the parameters of the four SSD telescopes. The experimental data of 25 MeV/u $^{86}\text{Kr} + ^{208}\text{Pb}$ is used in the analysis of this paper.

2.2. Energy calibration of the silicon strip detectors

Energy deposition (ϵ) of charged particles in silicon detectors is independent on particles, as long as the particles with $Z \leq 6$ is concerned. Energy calibration, in other words, is to get the linear function between ϵ and ADC channels (ch),

$$\epsilon = k \times ch + b \quad (1)$$

where k and b are linear fitting parameters. In the current experiment, energy calibration is performed strip-by-strip with both

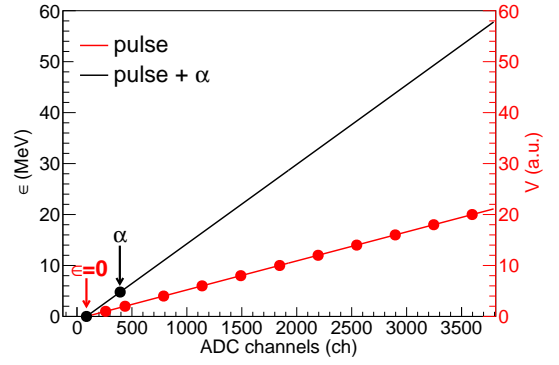


Fig. 2. (Color online) Results of energy calibration for one silicon strip. Data points of pulse calibration and the fitting results are shown in red color. The black dots represents the α source point and the “zero-energy” point, while the black line represents the final calibration.

pulse and ^{241}Am α source.

In pulse calibration, one can get the linear fitting parameters k' and b' of the following function between the input pulse amplitude (V) and ADC channels (ch),

$$V = k' \times ch + b' \quad (2)$$

Assuming V can be converted to the equivalent energy ϵ by $V = \beta\epsilon$, where β is a constant to be determined, one writes

$$\beta\epsilon = k' \times ch + b' \quad (3)$$

Here β can be fixed by an α energy point with $\beta = (k' \times ch(\alpha) + b')/\epsilon(\alpha)$, where $\epsilon(\alpha)$ and $ch(\alpha)$ are the energy and the ADC channel of the peak, respectively. The energy calibration is then determined as

$$\epsilon = \frac{k'}{\beta} \times ch + \frac{b'}{\beta} \quad (4)$$

Fig. 2 shows the results of the energy calibration of one silicon strip. The red points with the linear fit are the data with a precise pulse generator (ORTEC 419), showing excellent linearity. The black dots are the α point and the “zero-energy” point which is unchanged with the pulse calibration. The black line is the final calibration obtained from formula (4). The calibration quality is assured by the linearity of the pulse calibration. On the other hand, however, the uncertainty of the alpha source point can be magnified when going to high energy part, and a better way with multi α particles in a wide energy range can be found in [4].

2.3. Particle identification with $\Delta E - E$ method

2.3.1. Particle identification

Particle identification (PID) is of crucial importance in the detection of charged particles. Here we recall two conventional methods used to achieve PID. Both methods rely on the $\Delta E - E$ correlation. For one method, each isotope is recognized by the inclusive contour drawn *a priori*, as shown in Fig. 3 (a). For the other method, PID is achieved for each particle on $\Delta E - E$

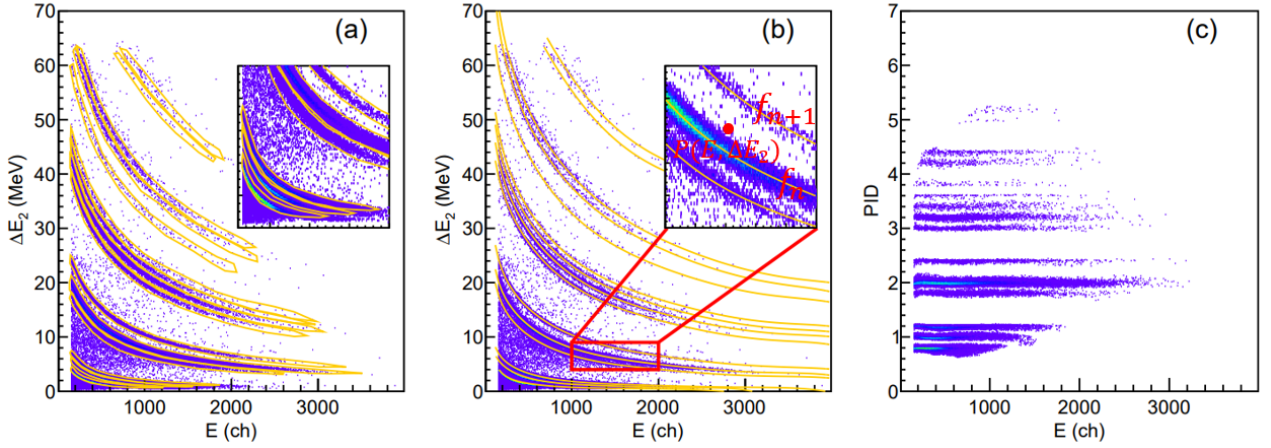


Fig. 3. (Color online) Particle identification of telescope No. 4. Panel (a) shows the inclusion contours for all the isotopes of a $\Delta E_2 - E$ scattering plot, where ΔE_2 and E are detected energies in the DSSSD and in the CsI(Tl) crystal, respectively. Panel (b) depicts the fitting curves of each isotope, and the inset shows the principle of the second PID method. Panel (c) shows the results of particle identification with isotope cuts shown in panel (a).

scattering plot by computing the distance from each individual point to the neighboring ridge curves following the isotopes. It is explained as following. First, one obtains the ridge curve by fitting the selected data points in the center of each isotope band using the following function,

$$f_n(x) = a_n^0 \cdot x^{-1} + a_n^1 \cdot x^0 + a_n^2 \cdot x^1 + a_n^3 \cdot x^2 + a_n^4 \cdot x^3 + a_n^5 \cdot x^4 + a_n^6 \cdot x^5 + a_n^7 \cdot x^6 \quad (5)$$

where $a_n^0 \sim a_n^7$ are eight fitting parameters, and different particles are denoted as different n values. Then, one defines the particle identification variable of a given isotope as [15]

$$\text{PID}_n = Z_n + 0.2(A_n - 2Z_n) \quad (6)$$

where Z_n and A_n are integers referring to the charge and the mass numbers of the particle represented by the fitting function or of a certain inclusion contour, respectively. Finally, the PID variable of every data point on the $\Delta E_2 - E$ scattering plot can be extracted from its distance to the ridge curves, e.g.,

$$\text{PID}(E, \Delta E_2) = \text{PID}_n + \frac{\Delta E_2 - f_n(E)}{f_{n+1}(E) - f_n(E)} \cdot (\text{PID}_{n+1} - \text{PID}_n) \quad (7)$$

Fig. 3 (b) depicts the fitting results for an example in the DSSSD-CsI(Tl) correlation plot. The inset shows the principle of the PID variable defined as formula (7). For this method, the isotope bands are straightened with formula (6) and (7), as shown in Fig. 3 (c). With this method, PID for SSSSD and DSSSD correlation can be achieved as well. Table 2 shows the mass resolution for α particles with the second PID method, indicating good particle identification capability of the telescopes as well as the high reliability of the PID procedure.

It is worth mentioning two limitations of using the formula (5) to fit each isotope. i) It is time-consuming for SSD telescope

Table 2: Mass resolution of the CSHINE telescopes obtained from the $\Delta E - E$ plots of α particles with particle identification. “A” and “ ΔA ” are the mean value and the 1σ standard deviation of the gaussian fit on the mass number distribution.

Tel. No.	$\Delta A/A$	
	SSSSD-DSSSD	DSSSD-CsI
1	0.041	0.042
2	0.039	0.039
3	0.049	0.059
4	0.045	0.062

array because each identification curve has to be drawn individually, and ii) the extrapolation to the region where the ridge curve of the low neighboring isotope does not reach likely deviates from the expected trend. Therefore, it will be very convenient if all the isotopes can be fitted simultaneously till higher energy. For example, Bethe formula has been used to fit the ridge curves for particle identification. Studies on this issue can be found in Refs. [15, 16].

2.3.2. Thickness correction for the thin silicon strip detectors

The energy loss of a particle traversing a thin silicon detector is approximately proportional to the detector thickness. It is important to correct the thickness non-uniformity of very thin silicon strip detectors, in order to improve the identification resolution with $\Delta E - E$ technique. Here, we make “relative” thickness correction with experimental data.

Relative thickness correction is based on the events with particles penetrating the thin SSSSD and stopped in the following DSSSD. For simplicity, we first select events with only one particle hitting both detectors. In principle, one can do the correction in the smallest unit, the individual pixel, but it requires high statistics in whole. Considering the variation of the uniformity is smooth, here the sensitive area is divided into 8×8 bins. In each bin, we draw the $\Delta E_1 - E_2$ histogram individually and pick a certain bin, which exhibits clear PID bands, as a ref-

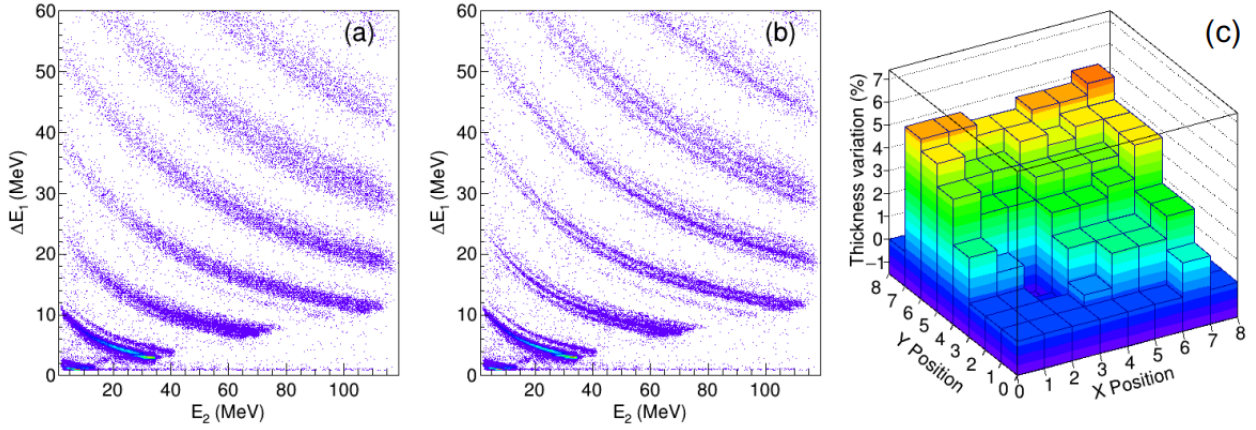


Fig. 4. (Color online) Panel (a) is a $\Delta E_1 - E_2$ scattering plot before thickness correction for the $110 \mu\text{m}$ ΔE_1 detector, and thickness of E_2 detector is $526 \mu\text{m}$. Panel (b) shows the 2D map after thickness correction for the ΔE_1 detector. Panel (c) depicts the “relative” thickness correction for the ΔE_1 detector.

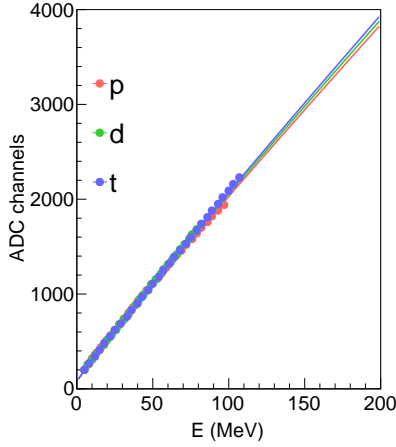


Fig. 5. (Color online) Energy calibration of hydrogen isotopes proton (red points), deuteron (green points), and triton (blue points) from CsI No. 8 in telescope No. 4. The curves represent the fitting results with formula (8).

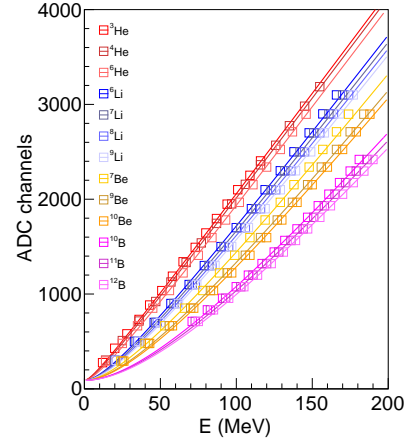


Fig. 6. (Color online) Energy calibration of heavy ions: $^2,3,6\text{He}$, $^6,7,8,9\text{Li}$, $^7,9,10\text{Be}$ and $^{10,11,12}\text{B}$ from CsI No. 8 in telescope No. 4. The corresponding curves represent the fitting results with formula (9).

erence. Then, for the rest bins, the thickness correction factor η for the SSSSD is varied from -0.05 to 0.10 with the step of 0.005 , and energy loss ΔE_1 in the SSSSD is corrected accordingly to be $\Delta E_1(1 + \eta)$. For each η value, a 2D histogram is filled and compared to the histogram of the reference bin. Finally, the thickness correction for each bin is determined with the η value if the corresponding histogram holds the best consistence with the referenced one. Fig. 4 (b) shows the 2D plot after the thickness correction for the $110 \mu\text{m}$ detector, the identification resolution is significantly improved when compared with the plot without correction as shown in Fig. 4 (a). Fig. 4 (c) is the “relative” thickness variation for the $110 \mu\text{m}$ SSSSD, which is covered by the range of from -1% to 6% . This method provides the relative correlation of the thickness of a thin ΔE detector with respect to a referenced bin. In order to get the absolute thickness correction, one should rely on in-beam tests, as introduced in Refs. [3, 17].

2.4. Energy calibration of the CsI(Tl) crystals

Energy calibration of CsI(Tl) crystals are more complicated than that of silicon since the light response of the CsI(Tl) crystal is non-linear and depends on the charge and mass of the particles as well as on the length of the crystal. Unlike energy calibration of silicon, it is inapplicable to calibrate CsI(Tl) crystals with low-energy α particle which is stopped near the surface of the crystals. Instead, the calibration of CsI(Tl) crystal can be carried out by using the $\Delta E - E$ method if the forward DSSSD with a well-defined thickness is calibrated. For particles penetrating the DSSSD (with energy loss ΔE_2) and stopped in the CsI(Tl) crystal, one can extract a set of data points on the ridge of each isotope band, as shown in Fig. 3 in particle identification. The kinetic energy of the incident particle E_k corresponding to each selected point can be deduced by a numerical inversion of Ziegler’s energy loss tables [18] with ΔE_2 (MeV) known in DSSSD. The residue energy in CsI(Tl) crystal can be

calculated as $E(\text{MeV}) = E_k - \Delta E_2$. With the set of data points for each isotope, the energy response of the CsI(Tl) can be calibrated. For $Z = 1$ isotopes, the calibration function is written as [19],

$$L(E, Z = 1, A) = a_0 + a_1 E^{\left(\frac{a_2 + A}{a_3 + A}\right)} \quad (8)$$

where a_0 is an offset, a_1 is a gain factor, A is the mass number of $Z = 1$ isotope, and a_2, a_3 are empirical non-linearity parameters.

For isotopes with $Z \geq 2$, a standard Horn's formula is used for calibration [20],

$$L(E, Z \geq 2, A) = a_0 + a_1 \left(E - a_2 A Z^2 \log \left(\frac{E + a_2 A Z^2}{a_2 A Z^2} \right) \right) \quad (9)$$

where a_0, a_1 and a_2 are parameters obtained from a simultaneous fit for all the heavy isotopes.

As shown in Fig. 5, the energy response for $Z = 1$ isotopes exhibits insignificant non-linearity and slight difference among the isotopes in the energy range of 0 – 100 MeV in accordance with the results in Ref. [19]. For the heavy isotopes from He to Boron, however, the non-linearity is increasingly pronounced depending on the species. With increasing the charge of the particle with the same energy, the response of the crystal is smaller, as shown in Fig. 6. The trends of the fitting curves are consistent with the results of HiRA10 detectors [19], and a detailed discussion on the energy calibration of CsI(Tl) crystals can be found therein.

3. Track reconstruction for the SSD-SSD-CsI telescope

In a CSHINE telescope, the firing position of an incident particle is determined by the crossing point of the front and the back strips of the DSSSD in the unit of pixel. The size of the pixel gives the position resolution. It is rather straightforward to recognize the track if only one particle hit the telescope. When multiplicity is larger than one, however, the track finding becomes much more complicated for the following reasons, i) the signal combination of the X strips and the Y strips on the DSSSD is not unique, ii) multi-track signals are hardly distinguishable with the charge sharing effect, and iii) hit can be missing with certain possibility.

3.1. Constraints

In order to recognize all the tracks impinging on the SSD telescope, one has to introduce a set of conditions to identify the real track signals. Considering the configuration of the CSHINE SSD telescope from top to bottom, e.g., the SSSSD, the DSSSD (with front- and back- side strips) and the 3×3 CsI(Tl) hodoscope. There are basically two types of conditions used for track reconstruction. One is the geometry condition marked by G_{O_1, O_2} , the other is the energy condition marked by E_{O_1, O_2} , where the subscripts O_1 and O_2 denote the two correlated objects that the condition is applied to. The geometry

Table 3: Geometrical map of the CSHINE telescopes. In each telescope, there are 16 channels for each silicon strip detectors and 3×3 CsI(Tl) crystals for the array.

CsI No. (N_{3A})	“2B” Strip No. (N_{2B})	“2F” Strip No. (N_{2F})	“1S” Strip No. (N_{1S})
0	$10 \leq N_{2B} \leq 15$	$10 \leq N_{2F} \leq 15$	
1	$10 \leq N_{2B} \leq 15$	$05 \leq N_{2F} \leq 10$	
2	$10 \leq N_{2B} \leq 15$	$00 \leq N_{2F} \leq 05$	
3	$05 \leq N_{2B} \leq 10$	$10 \leq N_{2F} \leq 15$	
4	$05 \leq N_{2B} \leq 10$	$05 \leq N_{2F} \leq 10$	$ N_{2B} - N_{1S} \leq 1$
5	$05 \leq N_{2B} \leq 10$	$00 \leq N_{2F} \leq 05$	
6	$00 \leq N_{2B} \leq 05$	$10 \leq N_{2F} \leq 15$	
7	$00 \leq N_{2B} \leq 05$	$05 \leq N_{2F} \leq 10$	
8	$00 \leq N_{2B} \leq 05$	$00 \leq N_{2F} \leq 05$	
DSSSD-CsI	$G_{3A, 2B}$	$G_{3A, 2F}$	$G_{2B, 1S}$
SSSSD-DSSSD			$G_{2B, 1S}$

conditions define the spatial match of one track in the SSD telescope, while the energy conditions define correspondingly the match of energy signals. Using “1S” to represent the SSSSD, “2F” (“2B”) to represent the front- (back-) side strips of the DSSSD and “3A” to represent the CsI hodoscope, respectively, one can list all the conditions as following:

- Geometrical constraints:
 - $G_{3A, 2B}$ (for DSSSD-CsI)
 - $G_{3A, 2F}$ (for DSSSD-CsI)
 - $G_{2B, 1S}$ (for both SSSSD-DSSSD and DSSSD-CsI)
- Energy constraints
 - $E_{3A, 2F}^{\text{iso}}$ (for DSSSD-CsI)
 - $E_{2F, 1S}$ (for DSSSD-CsI)
 - $E_{2B, 2F}$ (within the DSSSD)
 - $E_{2F, 1S}^{\text{iso}}$ (for SSSSD-DSSSD)

The superscript “iso” means that the condition is to match a certain isotope, see next.

Table 3 lists the detailed geometrical mapping of the CSHINE SSD telescope. For the particles stopped in a given unit of the CsI(Tl) crystal marked by N_{3A} , only the certain strips of the DSSSD, marked by N_{2F} and N_{2B} for the front and back strips, respectively, matches the geometrical condition $G_{3A, 2B}$ ($G_{3A, 2F}$). These two conditions are released for the particles stopped in the DSSSD. For example, as shown in the table, for the central CsI(Tl) unit with $N_{3A} = 4$, only the central part of the DSSSD with $05 \leq N_{2B} \leq 10$ and $05 \leq N_{2F} \leq 10$ satisfies the geometrical condition and delivers the signal of a same track. In addition, $G_{2B, 1S}$ is required for geometrical matching between the strips of the SSSSD and the back strips of the DSSSD. According to the configuration of the CSHINE telescope, the strips of the SSSSD and the back strips of the DSSSD are in parallel and numbered in the same direction. Given that the thickness of the silicon detector is very small compared to its distance to the

Table 4: Energy constraints of the CSHINE telescope No. 3. The thicknesses of the SSSSD and DSSSD are 110 μm and 526 μm , respectively.

Cases	Constraints	Descriptions
DSSSD-CsI	$E_{3A,2F}^{\text{iso}}$	$(E, \Delta E_{2F})$ inside an isotope cut
	$E_{2F,1S}$	$0.10 \leq \Delta E_{1S}/\Delta E_{2F} \leq 0.30$ ^a
SSSSD-DSSSD	$E_{2B,2F}$	$ (\Delta E_{2B} - \Delta E_{2F})/\Delta E_{2F} \leq 0.15$ ^b
	$E_{2F,1S}^{\text{iso}}$	$(E_{2F}, \Delta E_{1S})$ inside an isotope cut

^a Calculated results depending on the detector thicknesses.

^b Extracted from the experimental data.

target, one incident particle shall fire the SSSSD and the back-side of the DSSSD with the same or neighboring strip number, as constrained by $G_{2B,1S}$ of $|N_{2B} - N_{1S}| \leq 1$.

Table 4 lists the energy constraints for track decoding. For an effective event with the particle stopped in the CsI(Tl) crystal, three energy conditions are applied. i) The particle's energies $(E, \Delta E_2)$ should be inside banana-shaped polygon window corresponding to a certain isotope (discussed in sec. 2.3.1), which is denoted as $E_{3A,2F}^{\text{iso}}$. ii) the energies detected in the front-side (ΔE_{2F}) and back-side (ΔE_{2B}) of the DSSSD should be equal in ideal case. In reality, the relative difference of ΔE_{2F} and ΔE_{2B} should be smaller than a given value. This condition is represented by $E_{2B,2F}$. iii) A rather loose condition $E_{2F,1S}$ can be imposed as $\Delta E_{2F} > \Delta E_{1S}$, since the energy loss in the SSSSD and the DSSSD are roughly proportional to the detector thicknesses. Similarly, for the particle stopped in the DSSSD, the condition $E_{3A,2F}^{\text{iso}}$ can be released. Thus only two energy conditions are left. One is $E_{2F,1S}^{\text{iso}}$, referring that the data point $(E_{2F}, \Delta E_{1S})$ ought to be inside a certain isotope cut, the other is $E_{2B,2F}$, referring that the signal magnitude on the front and back strips of the DSSSD ought to be approximately equal.

Fig. 7 (a) shows the distribution of the ratio $\Delta E_1/\Delta E_2$, where ΔE_1 and ΔE_2 are energy losses of the particle penetrating two silicon detectors calculated by a numerical inversion of Ziegler's energy loss tables [18]. The thicknesses of the SSSSD and the DSSSD are 110 μm and 526 μm , respectively. It is shown that the peak of the distribution situates roughly at 20%, close to the thickness ratio of the SSSSD and the DSSSD. The box region represents the condition $E_{2F,1S}$. The relationship between ΔE_{2B} and ΔE_{2F} is obtained from experimental data and is shown in Fig. 7 (b), where the box region represents the condition $E_{2B,2F}$. Descriptions of all the energy constraints are listed in Table 4.

With the geometry conditions and energy conditions defined above, track recognition and event reconstruction can be conducted for the SSD-SSD-CsI telescopes of CSHINE. Since procedures in the two cases that the particles are stopped in the CsI hodoscope (DSSSD-CsI) and in the DSSSD (SSSSD-DSSSD) are quite different, methods of track recognition in this two cases are introduced in the following two sub-sections, respectively.

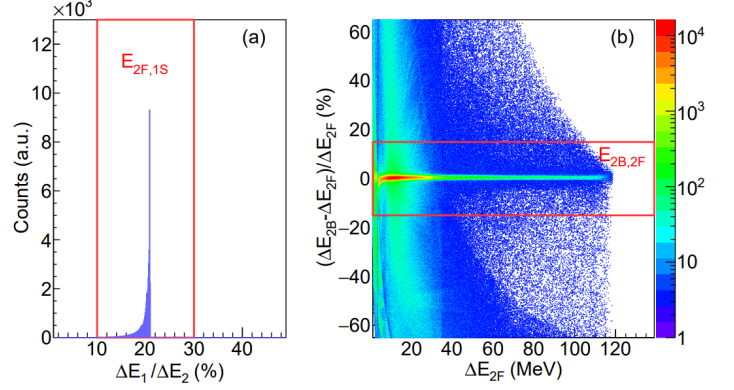


Fig. 7. (Color online) Panel (a) shows the ratio of the calculated energy losses of the particles penetrating the two silicon layers with the thicknesses of 110 μm and 526 μm respectively. Panel (b) shows the differences between the energy losses in the back- and front-side of the DSSSD extracted from the experimental data. The energy constraints $E_{2F,1S}$ and $E_{2B,2F}$ used for analysis are represented by the box regions, respectively.

3.2. Track reconstruction for the DSSSD-CsI

While track recognition for the event with track multiplicity $M_{\text{tr}} = 1$ in the telescope is easy, it is much more complicated when M_{tr} increases. In the following text, the method for track recognition with multiple tracks ($M_{\text{tr}} \geq 1$) is described, with special care of considering the charge sharing and multi track effects. In the analysis, it is assumed that the charge sharing effect occurs only between two adjacent strips. For simplicity, the track recognition procedure is started from the last detector layer ("3A") to the SSSSD layer ("1S"), as the multiplicity always decreases from first detector layer to the last layer. With all the preparation mentioned above, track reconstruction is to solve the following two questions:

- When to consider charge sharing and multi-hit effects?
- How to deal with charge sharing and multi-hit effects?

3.2.1. "When": track mode definition

In order to find the real tracks as efficiently as possible, track mode is classified following the flow diagram shown in Fig. 8 (a), the steps are explained below.

Step (a1) : For each event, to extract the multiplicities of all the detector layers, M_{3A}, M_{2B}, M_{2F} and M_{1S} , respectively. A real signal requires the amplitude to exceed a certain threshold, which is empirically set as above the pedestal for each individual channel.

Step (a2) : To determine the the number of candidate tracks (M) for each event with the geometrical constraints. It is an important step for track finding as only the geometrical constraints are used for determining the candidate tracks, while the energy constraints are used for track decoding in sec. 3.2.2. The candidate tracks are obtained by combining all the multiplicities of the four layers to satisfy $G_{3A,2B}, G_{3A,2F}$ and $G_{2B,1S}$ simultaneously. The event ratios of different M are listed in the " R_M " column of Table 5. As shown, track reconstruction is performed for events with $M = 1, 2, 3, 4$ and 6 ($M = 5$ is omitted as the percentage is much smaller).

Table 5: Modes included in track reconstruction for DSSSD-CsI of telescope No. 3. R_M is the ratio of events with different M values, and R_{Tr}^M represents the percentage of events with a certain track mode for a given M . $R_{\text{Dc}}^{\text{Tr}}$, $R_{\text{Sh}}^{\text{Tr}}$ and $R_{\text{Mh}}^{\text{Tr}}$ are the ratios of the decoded, charge sharing and multi-hit events for a given track mode, respectively. R_{Dc}^M , R_{Sh}^M and R_{Mh}^M are the sum over the track modes of $R_{\text{Dc}}^{\text{Tr}}$, $R_{\text{Sh}}^{\text{Tr}}$ and $R_{\text{Mh}}^{\text{Tr}}$, respectively. R_{Dc} , R_{Sh} and R_{Mh} are the sum over M of R_{Dc}^M , R_{Sh}^M and R_{Mh}^M , respectively. The cases with “—” are not included in the track decoding.

M	Ratio $R_M(\%)$	$R_{\text{Dc}}^M = \Sigma R_{\text{Tr}}^M R_{\text{Dc}}^{\text{Tr}}$ (%)	$R_{\text{Sh}}^M = \Sigma R_{\text{Tr}}^M R_{\text{Sh}}^{\text{Tr}}$ (%)	$R_{\text{Mh}}^M = \Sigma R_{\text{Tr}}^M R_{\text{Mh}}^{\text{Tr}}$ (%)	Track modes	Track Ratio $R_{\text{Tr}}^M(\%)$	Decoded $R_{\text{Dc}}^{\text{Tr}}(\%)$	Sharing $R_{\text{Sh}}^{\text{Tr}}(\%)$	Multi-hit $R_{\text{Mh}}^{\text{Tr}}(\%)$					
$M \geq 1$	100	—	—	—	—	—	—	—	—					
$M = 1$	69.10	93.92	—	—	Tr1 – 1111	100	93.92	—	—					
$M = 2$	17.73	87.98	29.98	4.86	Tr2 – 1112	5.07	82.83	18.48	—					
					Tr2 – 1121	54.09	84.80	40.23	—					
					Tr2 – 1211	11.35	86.85	64.18	—					
					Tr2 – 1212	7.23	86.09	0.02	—					
					Tr2 – 2111	0.46	74.72	—	—					
					Tr2 – 2121	7.10	96.97	—	60.22					
					Tr2 – 2212	0.92	95.75	—	63.61					
$M = 3$	2.35	84.13	17.29	7.90	Tr2 – 2222	13.79	99.51	—	—					
					Tr3 – 1113	0.17	88.46	—	—					
					Tr3 – 1131	17.06	78.12	38.70	—					
					Tr3 – 1212	9.73	84.68	9.41	—					
					Tr3 – 1213	1.09	81.44	—	—					
					Tr3 – 1312	2.76	88.65	31.21	—					
					Tr3 – 2121	7.59	87.34	—	49.00					
					Tr3 – 2131	8.57	71.93	—	48.74					
					Tr3 – 2221	2.41	91.33	—	—					
					Tr3 – 2222	23.00	99.29	—	—					
					Tr3 – 2223	1.86	98.24	—	—					
					Tr3 – 2232	13.27	99.01	40.79	—					
					Tr3 – 2322	4.65	97.61	75.14	—					
					Tr3 – 3222	1.82	81.36	—	—					
					Tr3 – 3333	0.26	100	—	—					
$M = 4$	6.05	80.28	14.52	1.10	Tr4 – 1122	4.40	54.93	21.38	—					
					Tr4 – 1212	9.91	88.37	88.36	—					
					Tr4 – 1221	13.35	79.81	36.12	—					
					Tr4 – 1222	22.08	72.68	—	—					
					Tr4 – 2122	1.38	89.67	—	79.89					
					Tr4 – 2221	8.48	95.15	—	—					
					Tr4 – 2222	33.74	97.95	—	—					
$M = 5$	0.36	—	—	—	Tr4 – 3333	0.05	94.74	—	—					
					Tr6 – 1123	0.06	14.29	—	—					
					Tr6 – 1132	1.20	35.51	—	—					
					Tr6 – 1222	14.68	64.26	—	—					
					Tr6 – 1223	1.49	71.35	—	—					
					Tr6 – 1231	3.42	64.47	—	—					
					Tr6 – 1232	6.10	66.52	—	—					
$M = 6$	1.77	71.07	—	0.74	Tr6 – 1322	3.81	67.43	—	—					
					Tr6 – 2122	0.93	99.07	—	79.44					
					Tr6 – 2221	5.63	92.44	—	—					
					Tr6 – 2222	26.55	98.04	—	—					
					Tr6 – 2223	2.22	94.14	—	—					
					Tr6 – 2232	11.81	92.86	—	—					
					Tr6 – 2322	6.11	93.60	—	—					
					Tr6 – 3333	0.41	91.49	—	—					
					Total	97.00	Decoded: $R_{\text{Dc}} = \Sigma R_M R_{\text{Dc}}^M = 88.59$, Sharing: $R_{\text{Sh}} = \Sigma R_M R_{\text{Sh}}^M = 6.60$, Multi-hit: $R_{\text{Mh}} = \Sigma R_M R_{\text{Mh}}^M = 1.13$							

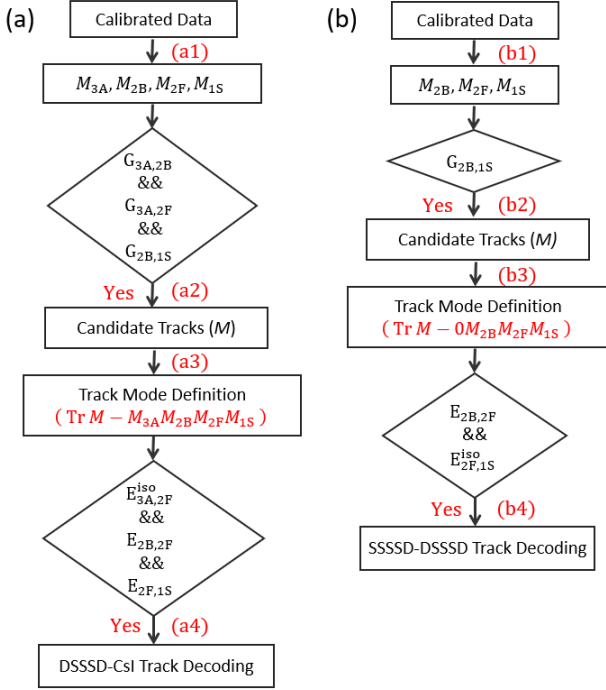


Fig. 8. Flow charts of track reconstruction for (a) DSSSD-CsI and for (b) SSSSD-DSSSD.

Step (a3) : To define the track modes with M and the multiplicities, denoted as “ $TrM - M_{3A}M_{2B}M_{2F}M_{1S}$ ”. For $M \geq 1$, one has $1 \leq M_{3A} \leq M$, $1 \leq M_{2B} \leq M$, $1 \leq M_{2F} \leq M$ and $1 \leq M_{1S} \leq M$, and there are maximally M^4 different track modes in total. However, it is found that the number of the effective modes are far less than M^4 . In track decoding, we selected the top modes as shown in the “Track modes” column in Table 5.

With the track modes well-defined, one can decode every mode according to the characteristics of the data and identify the charge sharing and multi-hit effects.

3.2.2. “How”: track mode decoding

For DSSSD-CsI, a track is well-defined when both $E_{3A,2F}^{iso}$ and $E_{2B,2F}$ are true, while $E_{2F,1S}$ is only used to cross check the energy loss of the particle in the first silicon layer. The cases of track decoding are listed as follows:

i) Consider charge sharing effect. In the track decoding, it is assumed that charge sharing only happens between two adjacent strips. For $M = 2$, it is easy to find the track with charge sharing. We take one Tr2-1211 event for an example of a charge sharing event, as shown in Table 6. This is an event with $M_{2B} = 2$ while $M_{3A} = M_{2F} = M_{1S} = 1$. The number of candidates is $M = 2$. It is shown that the sum of the energy losses in the two neighboring strips 8 and 9 in “2B” layer is close to the energy loss in the single strip 13 in “2F”, which satisfies the energy condition $E_{2B,2F}$. If $E_{2F,3A}^{iso}$ is also true, then one real track is finally determined. For even larger M , we have to find out two tracks with adjacent strips so that we can consider charge sharing effect. The example is also shown in Ta-

ble 6 by a Tr4-1212 event. The number of track candidates is $M = 4$, and two firing strips are found in both 2B and 1S layers. However, charge sharing in “2B” layer can be identified by comparing track candidate No. 2 and No. 3 (or No. 1 and No. 4), indicating that there is one valid track in this mode. The ratios of charge sharing for the track modes are listed in the R_{Sh}^{Tr} column in Table 5.

Table 6: Data characteristics of some typical track modes.

Charge sharing: Tr2 – 1211								
Track No.	N_{3A}	N_{2B}	N_{2F}	N_{1S}	E_{3A} (ch)	ΔE_{2B} (MeV)	ΔE_{2F} (MeV)	ΔE_{1S} (MeV)
1	3	8	13	9	1273	58.15	98.12	13.40
2	3	9	13	9	1273	36.58	98.12	13.40
Charge sharing: Tr4 – 1212								
Track No.	N_{3A}	N_{2B}	N_{2F}	N_{1S}	E_{3A} (ch)	ΔE_{2B} (MeV)	ΔE_{2F} (MeV)	ΔE_{1S} (MeV)
1	6	2	15	2	1014	19.62	26.78	4.21
2	6	2	15	3	1014	19.62	26.78	1.63
3	6	3	15	2	1014	7.18	26.78	4.21
4	6	3	15	3	1014	7.18	26.78	1.63
Multi-hit: Tr2 – 2212								
Track No.	N_{3A}	N_{2B}	N_{2F}	N_{1S}	E_{3A} (ch)	ΔE_{2B} (MeV)	ΔE_{2F} (MeV)	ΔE_{1S} (MeV)
1	5	6	2	6	1163	12.01	38.45	1.55
2	8	3	2	3	1890	26.56	38.45	3.49
Multi-hit: Tr4 – 2122								
Track No.	N_{3A}	N_{2B}	N_{2F}	N_{1S}	E_{3A} (ch)	ΔE_{2B} (MeV)	ΔE_{2F} (MeV)	ΔE_{1S} (MeV)
1	7	3	9	3	1670	16.12	9.98	1.91
2	7	3	9	4	1670	16.12	9.98	0.90
3	8	3	2	3	3444	16.12	6.01	1.91
4	8	3	2	4	3444	16.12	6.01	0.90
No charge sharing or multi-hit: Tr4 – 2222 ^I								
Track No.	N_{3A}	N_{2B}	N_{2F}	N_{1S}	E_{3A} (ch)	ΔE_{2B} (MeV)	ΔE_{2F} (MeV)	ΔE_{1S} (MeV)
1	5	8	0	8	822	14.83	14.77	1.90
2	5	8	4	8	822	14.83	37.52	1.90
3	8	3	0	3	1012	37.57	14.77	5.48
4	8	3	4	3	1012	37.57	37.52	5.48
No charge sharing or multi-hit: Tr4 – 2222 ^{II}								
Track No.	N_{3A}	N_{2B}	N_{2F}	N_{1S}	E_{3A} (ch)	ΔE_{2B} (MeV)	ΔE_{2F} (MeV)	ΔE_{1S} (MeV)
1	2	12	0	12	724	16.34	16.93	1.95
2	2	12	1	12	724	16.34	16.31	1.95
3	5	9	0	9	641	17.04	16.93	2.00
4	5	9	1	9	641	17.04	16.31	2.00
Cross check ΔE_{1S} : Tr2 – 2222								
Track No.	N_{3A}	N_{2B}	N_{2F}	N_{1S}	E_{3A} (ch)	ΔE_{2B} (MeV)	ΔE_{2F} (MeV)	ΔE_{1S} (MeV)
1	2	13	3	13	1573	9.99	9.97	1.44
2	3	5	13	5	1264	12.84	12.80	19.34

ii) Consider multi-hit effect. When “multi-hit” is mentioned, it refers that there are two (or more) particles hitting the same strip. In the analysis, events with two or more particles hitting the same CsI(Tl) crystal are discarded as we can not get the real deposited energy in the crystal in this case. In Table 6, e.g., Tr2-2212 is an event with two candidate tracks which are all valid, with the two particles hitting the same strip on the “2F” layer. In such case E_{2B} is used instead of E_{2F} for particle

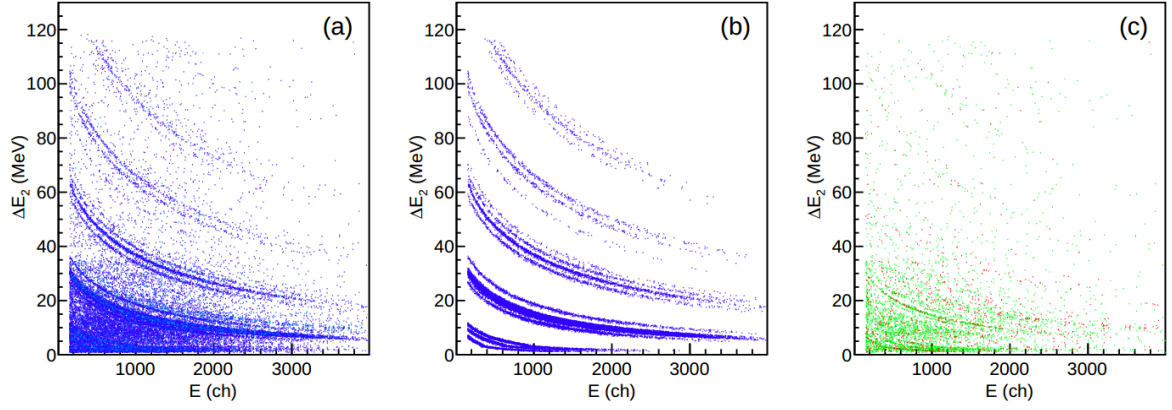


Fig. 9. Results of track reconstruction for DSSSD-CsI of telescope No. 3. Panel (a) shows the results for the tracks with $M = 1, 2, 3, 4$, and 6 . Panel (b) represents the results after track decoding, and panel (c) shows the lost events.

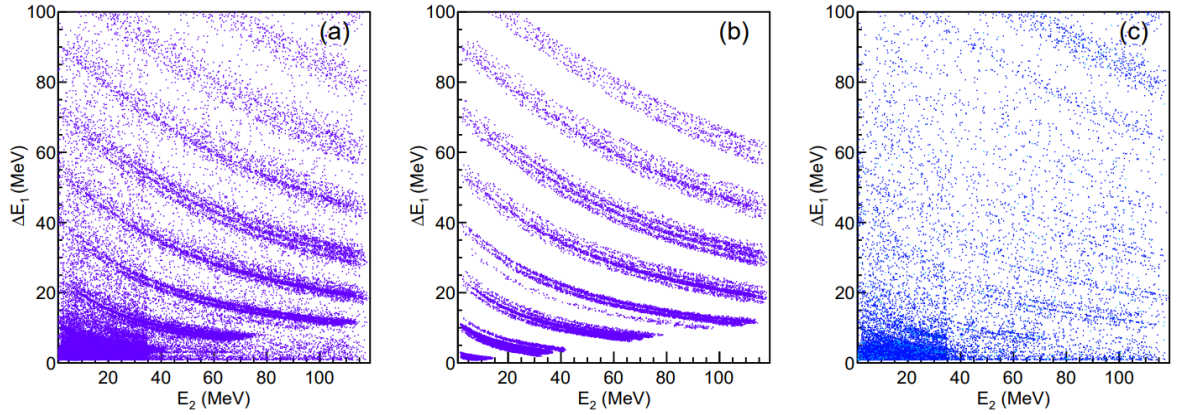


Fig. 10. Results of track reconstruction for SSSSD-DSSSD of telescope No. 3. Panel (a) shows the results for the tracks with $M = 1, 2, 3, 4$, and 6 . Panel (b) represents the results after track decoding, and panel (c) shows the lost events.

identification when double-hit happens on the front side of the DSSSD. For larger M , we have to try every two tracks to find out the positions of multi-hit. To see Tr4-2122 in Table 6 for another example, track No. 1 and No. 4 (or track No. 2 and No. 3) are valid tracks with two particles hitting the same strip on the back-side “2B” of the DSSSD. The ratios of multi-hit events for all the track modes are listed in the $R_{\text{Mh}}^{\text{Tr}}$ column in Table 6.

iii) No charge sharing or double-hit effects. In most cases, instead of considering charge sharing and double-hit effects, we try to find out the real tracks with $E_{3A,2F}^{\text{iso}}$ and $E_{2B,2F}$ directly. The number of valid tracks is determined by the smallest multiplicity among M_{3A} , M_{2B} and M_{2F} . As expected, there will be one real track for Tr2-1212 if no charge sharing or multi-hit happens. For larger M , we can use $E_{2B,2F}$ to find out the valid tracks. For example, for the event Tr4 – 2222^I in Table 6, it is clear that track No. 1 and No. 4 are two valid tracks. However, it is very difficult to find out the real tracks if the two particle hitting the DSSSD have the close energies, as shown the second Tr4 – 2222^{II} in Table 6. In this case, the events are currently discarded as the statistics of this track mode is rather low.

iv) Cross check the energy loss ΔE_{1S} in “1S” layer. From i) to iii), we can determine the valid tracks, but we have to

cross check ΔE_{1S} as well to finalize the track reconstruction for DSSSD-CsI. See Tr2-2222 in Table 6 for example, track No. 1 is a valid track and satisfied with $E_{2F,1S}$ as listed in Table 4. Track No. 2 is also a valid track since it is satisfied with both $E_{3A,2F}^{\text{iso}}$ and $E_{2B,2F}$, but $E_{2F,1S}$ is not true due to the large energy loss in the “1S” layer, which possibly due to a heavy fragment stopped in the same “1S” strip. In this case, as long as a valid track is identified, ΔE_{1S} can be recalculated by the following procedures: 1) the charge (Z) and mass (A) of the particle can be obtained from $E_{3A,2F}^{\text{iso}}$; 2) the energy of the particle impinging the DSSSD E_2^{imp} can be deduced by the numerical inversion of Ziegler’s energy loss tables [18]; 3) the energy of the particle impinging the SSSSD E_1^{imp} can be also deduced similarly; 4) the particle’s energy loss in the SSSSD is $E_1^{\text{imp}} - E_2^{\text{imp}}$. Finally, the total kinetics energy of the impinging particle is $E_{\text{tot}} = \Delta E_1 + \Delta E_2 + E$.

Based on the above procedures, we can decode the tracks effectively. As shown in the last row in Table 6, the total efficiency of the track decoding for DSSSD-CsI is 88.59 %, and the ratios of charge sharing and multi-hit are 6.60 % and 1.13 %, respectively. Comparing with the test results with an α source, where the ratio of charge sharing is found to be less than 1 %,

Table 7: Modes included in track reconstruction for SSSSD-DSSSD of telescope No. 3. R_M is the ratio of events with different M values, and R_{Tr}^M represents the percentage of events with a certain track mode for a given M . R_{Dc}^{Tr} , R_{Sh}^{Tr} and R_{Mh}^{Tr} are the ratios of the decoded, charge sharing and multi-hit events for a given track mode, respectively. R_{Dc}^M , R_{Sh}^M and R_{Mh}^M are the sum over the track modes of R_{Dc}^{Tr} , R_{Sh}^{Tr} and R_{Mh}^{Tr} , respectively. R_{Dc} , R_{Sh} and R_{Mh} are the sum over M of R_{Dc}^M , R_{Sh}^M and R_{Mh}^M , respectively. The cases with “—” are not included in the track decoding.

M	Ratio $R_M(\%)$	$R_{Dc}^M = \Sigma R_{Tr}^M R_{Dc}^{Tr}$ (%)	$R_{Sh}^M = \Sigma R_{Tr}^M R_{Sh}^{Tr}$ (%)	$R_{Mh}^M = \Sigma R_{Tr}^M R_{Mh}^{Tr}$ (%)	Track modes	Track Ratio $R_{Tr}^M(\%)$	Decoded $R_{Dc}^{Tr}(\%)$	Sharing $R_{Sh}^{Tr}(\%)$	Multi-hit $R_{Mh}^{Tr}(\%)$
$M \geq 1$	100	—	—	—	—	—	—	—	—
$M = 1$	76.28	80.63	—	—	Tr1 – 0111	100	80.63	—	—
$M = 2$	14.71	77.02	68.51	0.58	Tr2 – 0112 Tr2 – 0121 Tr2 – 0211 Tr2 – 0212	7.28 67.44 23.41 1.87	81.72 75.53 80.01 74.87	43.77 68.89 80.56 0.13	— — — 31.19
$M = 3$	0.80	67.17	58.79	1.51	Tr3 – 0113 Tr3 – 0131 Tr3 – 0212 Tr3 – 0213 Tr3 – 0311 Tr3 – 0312 Tr3 – 0313	0.61 82.05 8.76 1.19 0.65 6.53 0.19	64.29 66.61 69.28 76.92 12.50 75.18 80.00	— 65.53 47.71 — 12.51 11.68 —	— — 9.15 3.85 — 9.49 20.00
$M = 4$	5.69	87.03	15.80	2.34	Tr4 – 0122 Tr4 – 0212 Tr4 – 0221 Tr4 – 0222	4.84 1.52 17.54 74.75	71.81 76.37 68.67 94.11	34.01 54.43 75.98 —	41.06 23.21 — —
$M = 5$	0.02	—	—	—	—	—	—	—	—
$M = 6$	1.31	78.41	6.86	—	Tr6 – 0222 Tr6 – 0223 Tr6 – 0231 Tr6 – 0232 Tr6 – 0322	20.01 7.10 9.90 31.64 26.41	84.35 91.22 54.89 84.85 86.23	— — 69.29 — 70.29	— — — — —
Total	98.79	Decoded: $R_{Dc} = \Sigma R_M R_{Dc}^M = 79.35$, Sharing: $R_{Sh} = \Sigma R_M R_{Sh}^M = 11.54$, Multi-hit: $R_{Mh} = \Sigma R_M R_{Mh}^M = 0.23$							

the charge sharing effect is much more obvious in the beam experiment, indicating this effect must be included in data analysis. Fig. 9 (a) and (b) present the $\Delta E_2 - E$ scattering plot of telescope No. 3 before and after the track decoding. For a comparison, Fig. 9 (c) presents the results of the leftover events. It is evident that the track decoding efficiency is high.

3.3. Track reconstruction for the SSSSD-DSSSD

As shown in Fig. 8 (b), the procedures of track reconstruction for SSSSD-DSSSD is similar to DSSSD-CsI, but they are different in three aspects:

- Only $G_{2B,1S}$ is used to determine candidate tracks (M), because the CsI(Tl) hodoscope is not fired.
- The track modes is defined as “Tr $M - 0M_{2B}M_{2F}M_{1S}$ ” for the same reason.
- Both $E_{2B,2F}$ and $E_{2F,1S}^{iso}$ are used for track decoding.

The maximum number of track modes is M^3 , much less than those for DSSSD-CsI. Table 7 shows the information of track decoding for SSSSD-DSSSD. As shown in the last row in Table 7, the efficiency of track decoding for SSSSD-DSSSD is 79.35 %, which is smaller than that for DSSSD-CsI. There are mainly

two reasons for the lower efficiency, i) many heavy fragments are stopped in the first SSSSD layer and increases the multiplicity in the layer of SSSSD (M_{1S}) and ii) the tracks penetrating the two SSDs but hitting to the materials in the gaps (about 1 mm wide) between the CsI crystals are mostly discarded. For the latter case, the particle may penetrates the DSSSD and escapes without energy response in the CsI crystals. These events are included in the $\Delta E_1 - E_2$ plot, but are discarded in track decoding particularly in the area of low ΔE_1 , which may decrease the efficiency. The ratios of event with charge sharing and double-hit are 11.54 % and 0.23 %, respectively. Fig. 10 shows the results of track reconstruction for SSSSD-DSSSD of telescope No. 3. Comparing Fig. 10 (b) and Fig. 10 (c), it can be found that most of the tracks are effectively reconstructed with this method.

4. Coordinate transformation

Once the track is recognized, the position coordinate can be deduced from the geometry of the strips in the detector’s frame. Since it is usual to conduct physical analysis in the laboratory

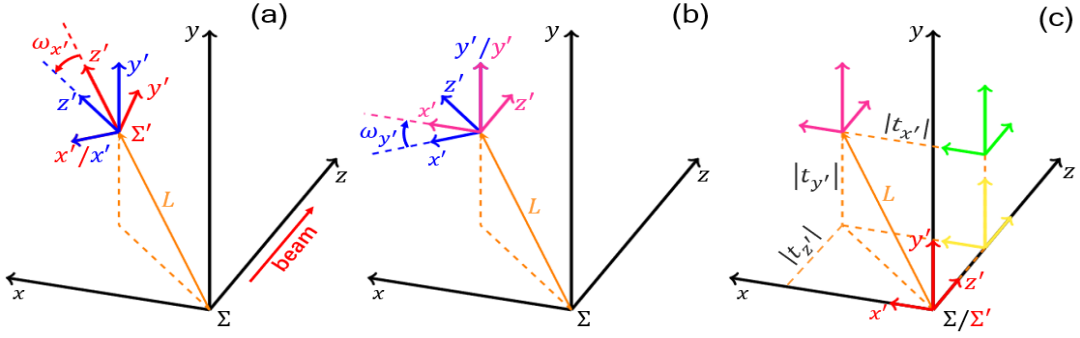


Fig. 11. (Color online) Sketch of coordinate transformation. Panel (a) and (b) represent $\hat{R}_{x'}(\omega_{x'})$ and $\hat{R}_{y'}(\omega_{y'})$ operation respectively, and panel (c) shows the translation operation along the x' , y' and z' axes, respectively.

frame, coordinate transformation from the detector's frame to the laboratory frame is required. Here we focus on the passive transformation method, i.e., the vector is fixed and the reference frame is rotated.

Let's recall briefly the math of the coordinate transformation. Consider the coordinates of a fixed vector \mathbf{A} in two different frames of reference Σ and Σ' , one writes

$$|A\rangle_{\Sigma} = \sum_n |n\rangle \langle n|A\rangle = \sum_n A_n |n\rangle \quad (10)$$

$$|A\rangle_{\Sigma'} = \sum_{n'} |n'\rangle \langle n'|A\rangle = \sum_{n'} A_{n'} |n'\rangle \quad (11)$$

where $|n\rangle$ and $|n'\rangle$ are the basis vectors of the corresponding frames, and A_n and $A_{n'}$ are the coordinates. By comparing (10) and (11), one obtains

$$\begin{aligned} A_n &= \langle n|A\rangle = \sum_{n'} \langle n|n'\rangle \langle n'|A\rangle \\ &= \sum_{n'} \langle n|n'\rangle A_{n'} = \sum_{n'} S_{nn'} A_{n'} \end{aligned} \quad (12)$$

where $S_{nn'}$ is the element of the transformation matrix from Σ' to Σ ($S_{\Sigma' \rightarrow \Sigma}$).

In practice, transformation matrix can be obtained from rotation and translation operation, as shown in Fig. 11. The detector's frame and the laboratory frame are defined as Σ' and Σ , shown in red and black, respectively. Initially, z' is along the direction from the target to the center of the SSD telescope, which is perpendicular to the incident plane of the detector, while x' and y' are along the front and back strips of the DSSSD, respectively. The three steps of transformation is depicted by panel (a)-(c). First, one rotates the detector around its x' axis by an angle $\omega_{x'}$, denoted by the operator $\hat{R}_{x'}(\omega_{x'})$, so that the y' becomes vertical as y axis in laboratory. Then detector frame is rotated around its y' axis by an angle $\omega_{y'}$ ($\hat{R}_{y'}(\omega_{y'})$), so that x' becomes horizontal. Finally, we translate the detector reference frame along its x' , y' and z' axes, denoted by the operators $\hat{T}(t_{x'})$, $\hat{T}(t_{y'})$ and $\hat{T}(t_{z'})$, respectively. Therefore, (12) turns to be

$$|A\rangle_{\Sigma} = \hat{T}(t_{z'}) \hat{T}(t_{y'}) \hat{T}(t_{x'}) \hat{R}_{y'}(\omega_{y'}) \hat{R}_{x'}(\omega_{x'}) |A\rangle_{\Sigma'} \quad (13)$$

Mathematically, we can describe the rotation in 3-D space with a 3×3 matrix. One can add an additional dimension if translation operation follows. Indeed, a 4×4 matrix is introduced to describe the combination of rotation and translation, and (13) is then extended as

$$\begin{aligned} \begin{pmatrix} A_x \\ A_y \\ A_z \\ 1 \end{pmatrix} &= \begin{pmatrix} 1 & 0 & 0 & 0 \\ 0 & 1 & 0 & 0 \\ 0 & 0 & 1 & t_{z'} \\ 0 & 0 & 0 & 1 \end{pmatrix} \begin{pmatrix} 1 & 0 & 0 & 0 \\ 0 & 1 & 0 & t_{y'} \\ 0 & 0 & 1 & 0 \\ 0 & 0 & 0 & 1 \end{pmatrix} \begin{pmatrix} 1 & 0 & 0 & t_{x'} \\ 0 & 1 & 0 & 0 \\ 0 & 0 & 1 & 0 \\ 0 & 0 & 0 & 1 \end{pmatrix} \begin{pmatrix} \cos \omega_{y'} & 0 & -\sin \omega_{y'} & 0 \\ 0 & 1 & 0 & 0 \\ \sin \omega_{y'} & 0 & \cos \omega_{y'} & 0 \\ 0 & 0 & 0 & 1 \end{pmatrix} \begin{pmatrix} 1 & 0 & 0 & 0 \\ 0 & \cos \omega_{x'} & \sin \omega_{x'} & 0 \\ 0 & -\sin \omega_{x'} & \cos \omega_{x'} & 0 \\ 0 & 0 & 0 & 1 \end{pmatrix} \begin{pmatrix} A_{x'} \\ A_{y'} \\ A_{z'} \\ 1 \end{pmatrix} \\ &= \begin{pmatrix} 1 & 0 & 0 & t_{x'} \\ 0 & 1 & 0 & t_{y'} \\ 0 & 0 & 1 & t_{z'} \\ 0 & 0 & 0 & 1 \end{pmatrix} \begin{pmatrix} \cos \omega_{y'} & \sin \omega_{x'} \sin \omega_{y'} & -\cos \omega_{x'} \sin \omega_{y'} & 0 \\ 0 & \cos \omega_{x'} & \sin \omega_{x'} & 0 \\ \sin \omega_{y'} & -\sin \omega_{x'} \cos \omega_{y'} & \cos \omega_{x'} \cos \omega_{y'} & 0 \\ 0 & 0 & 0 & 1 \end{pmatrix} \begin{pmatrix} A_{x'} \\ A_{y'} \\ A_{z'} \\ 1 \end{pmatrix} \\ &= \begin{pmatrix} \cos \omega_{y'} & \sin \omega_{x'} \sin \omega_{y'} & -\cos \omega_{x'} \sin \omega_{y'} & t_{x'} \\ 0 & \cos \omega_{x'} & \sin \omega_{x'} & t_{y'} \\ \sin \omega_{y'} & -\sin \omega_{x'} \cos \omega_{y'} & \cos \omega_{x'} \cos \omega_{y'} & t_{z'} \\ 0 & 0 & 0 & 1 \end{pmatrix} \begin{pmatrix} A_{x'} \\ A_{y'} \\ A_{z'} \\ 1 \end{pmatrix} \end{aligned} \quad (14)$$

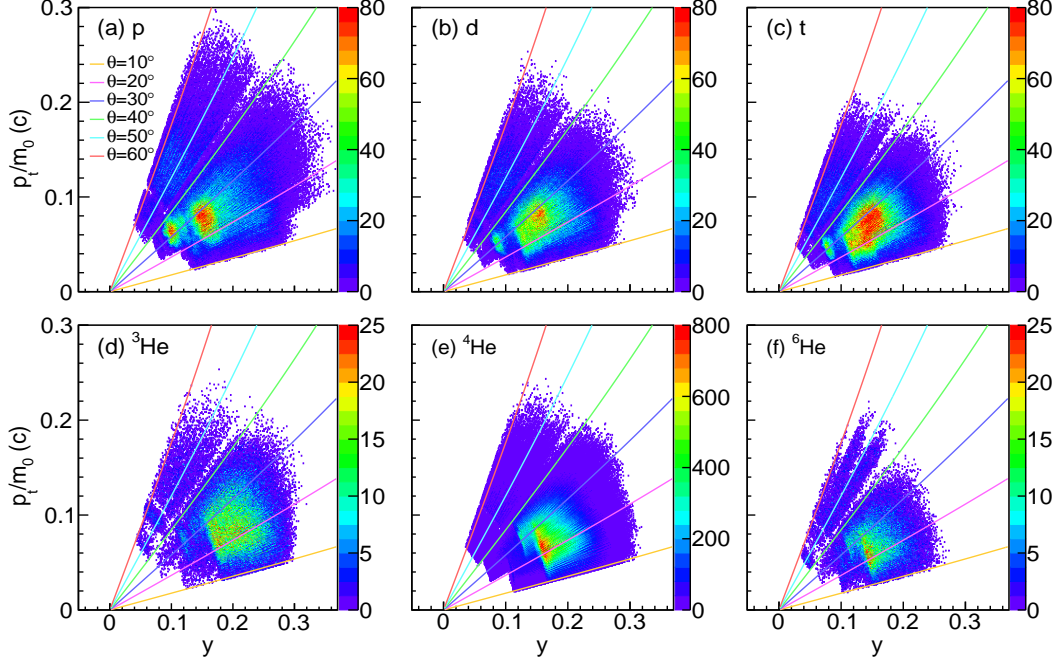


Fig. 12. (Color online) Phase space distribution of the LCPs measured by the CSHINE telescope array used in the $^{86}\text{Kr} + ^{208}\text{Pb}$ reactions at 25 MeV/u [14]. From (a) to (f) shows the results of p, d, t, ^3He , ^4He and ^6He , respectively.

Here, $t_{x'}$, $t_{y'}$ and $t_{z'}$ are the translation variables from the origin of Σ' to that of Σ . Eventually, from the position where the detector is fixed on the mechanic frame, one obtains the values of $\omega_{x'}$, $\omega_{y'}$ and the distance L from the geometrical center of the

detector to the target. Note that the sign of the rotation angle is determined by the right-hand rule. Rewriting $t_{x'}$, $t_{y'}$ and $t_{z'}$ with L , $\omega_{x'}$ and $\omega_{y'}$, (14) becomes

$$\begin{pmatrix} A_x \\ A_y \\ A_z \\ 1 \end{pmatrix} = \begin{pmatrix} \cos \omega_{y'} & \sin \omega_{x'} \sin \omega_{y'} & -\cos \omega_{x'} \sin \omega_{y'} & L \cos \omega_{x'} \sin \omega_{y'} \\ 0 & \cos \omega_{x'} & \sin \omega_{x'} & -L \sin \omega_{x'} \\ \sin \omega_{y'} & -\sin \omega_{x'} \cos \omega_{y'} & \cos \omega_{x'} \cos \omega_{y'} & -L \cos \omega_{x'} \cos \omega_{y'} \\ 0 & 0 & 0 & 1 \end{pmatrix} \begin{pmatrix} A_{x'} \\ A_{y'} \\ A_{z'} \\ 1 \end{pmatrix} \quad (15)$$

Eq. (15) is the final result of coordinate transformation. We notice that the sign of $t_{x'} = L \cos \omega_{x'} \sin \omega_{y'}$ is determined by the sign of $\omega_{y'}$, while the sign of $t_{y'} = -L \sin \omega_{x'}$ is determined by $\omega_{x'}$. It shall be noted that the rotation matrix of the passive transformation is the inversion of the passive transformation's matrix, and the sign of $t_{z'}$ is determined by the position of the detector relative to the target, e.g., $t_{z'}$ is $-L \cos \omega_{x'} \cos \omega_{y'}$ in this work since the detectors are placed at forward hemisphere. Generally, we choose the front surface of the DSSSD as the $x' - y'$ plane, and take $A_{z'} = 0$. The position of the impinging particle in this plane, e.g., $A_{x'}$ and $A_{y'}$, is derived from the strip numbers of the back- and front-sides of the DSSSD. Then one obtains the particle's coordinates in the laboratory frame with eq. (15).

5. Results

Fig. 12 presents the phase space distribution for the CSHINE telescopes in the experiment with $^{86}\text{Kr} + ^{208}\text{Pb}$ at 25 MeV/u [14]. The rapidity, the transverse momentum and the mass of

the particle are denoted as y , p_t and m_0 . The curves are the results of p_t/m_0 as the function of θ and y as ,

$$\frac{p_t}{m_0} = \frac{\tanh y \cdot \tan \theta}{\sqrt{1 - (\tanh y / \cos \theta)^2}} \quad (16)$$

It shows that the telescopes can measure light charged particles in a wide angular range from $\theta = 10^\circ - 60^\circ$. For the current beam energies, the emission of light charged particles in the angular range is contributed mainly by the intermediate velocity source and carries the information of the transport of the isospin degree of freedom [21]. Therefore CSHINE with the full configuration of SSD telescopes provides opportunities for physics studies such as the constraint of nuclear equation of state via the isospin composition of the particles as well as the HBT chronology for different isotopes in heavy ion reactions at Fermi energies [22, 23].

6. Summary

In this paper, a novel method of track recognition for the CSHINE SSD telescopes is described. The procedure includes detector calibration, track reconstruction and coordinate transformation. The silicon strip detectors are calibrated using pulse and α source, while the CsI(Tl) crystals are calibrated using the $\Delta E_2 - E$ scattering plot after PID is achieved. A novel practical method is invented for track reconstruction by a detailed analysis on the track mode, which are defined by the number of candidate tracks and the hit multiplicities in the four layers of the telescope. Through track decoding algorithm, one can discriminate the charge sharing and multi-hit effects quantitatively. High tracking efficiency of 88.59% and 79.35% is achieved in SSSSD-DSSSD and DSSSD-CsI combinations, respectively. The procedure of coordinate transformation from the detector's frame to the laboratory frame is briefly described for completeness. The phase space distribution for the LCPs with $Z \leq 2$ are obtained, demonstrating that CSHINE telescopes can measure the LCPs in the range of $\theta = 10^\circ$ to 60° in laboratory and provide opportunities for future physical studies, such as the constraint of nuclear equation of state as well as HBT chronology in heavy ion reactions at Fermi energies.

Acknowledgments

This work is supported by the National Natural Science Foundation of China under Grants Nos. 11875174, 11961131010, and 11890712, the Ministry of Science and Technology under Grant No. 2020YFE0202001, the Initiative Scientific Research Program of Tsinghua University, and by the

Heavy Ion Research Facility in Lanzhou (HIRFL). The authors acknowledge the gas detector group and the RIBLL group at the Institute of Modern Physics, Chinese Academy of Sciences, for offering local help in experiment and the machine staff for delivering the beam.

References

- [1] J. Pouthas, et al., Nucl. Instr. Meth. A 357 (1995) 418.
- [2] O. Lopez, et al., Nucl. Instr. Meth. A 884 (2018) 140.
- [3] B. Davin, et al., Instr. Meth. A 473 (2001) 302.
- [4] M.S. Wallace, et al., Nucl. Instr. Meth. A 583 (2007) 302.
- [5] N. Le Neindre, et al., Nucl. Instr. Meth. A 490 (2002) 251.
- [6] E. Pollacco, et al., Eur. Phys. J. A 25 (2005) 287.
- [7] G. Verde, et al., J. Phys.: Conf. Ser. 420 (2013) 012158.
- [8] L. Acosta, et al., J. Phys.: Conf. Ser. 730 (2016) 012001.
- [9] R. Bougault, et al., Eur. Phys. J. A 50 (2014) 47.
- [10] Samir Kundu, et al., Nucl. Instr. Meth. A 943 (2019) 162411.
- [11] Q.H. Wu, et al. Phys. Lett. B 797 (2019) 134808.
- [12] Q.H. Wu, et al., Phys. Lett. B 811 (2020) 135865.
- [13] Y.J. Wang, et al., Nucl. Sci. Tech. 32 (2021) 4.
- [14] F.H. Guan, et al., Nucl. Instr. Meth. A 1011 (2021) 165592.
- [15] L. Tassan-Got, Nucl. Instr. Meth. B 194 (2002) 503.
- [16] J. Blicharska et al., LNS report 2005.
- [17] Qiang Liu, et al., Nucl. Instr. Meth. A 897 (2018) 100.
- [18] J. Ziegler, et al., The Stopping and Range of Ions in Matter, Pergamon Press, New York, 1985.
- [19] D. Dell'Aquila, et al., Nucl. Instr. Meth. A 929 (2019) 162.
- [20] D. Horn, et al., Nucl. Instr. Meth. A 320 (1992) 273.
- [21] Yan Zhang, et al., Phys. Rev. C 95, 041602 (2017).
- [22] Yijie Wang, et al., The Emission Order of Hydrogen Isotopes via Correlation Functions in 30 MeV/u Ar+Au Reactions (In process).
- [23] Xinyue Diao, et al., Properties of the fast fission and the coincident emissions of lightcharged particles in $40\text{Ar}+197\text{Au}$ reactions at 30 MeV/u, arXiv:2110.02389.